MAGNETIC EPITAXIAL LAYERS

MAGNETIC INTERACTIONS AS STUDIED BY NEUTRON SCATTERING

Magnetic devices comprised of magnetic thin films or multilayers are the current standards for information storage and retrieval in modern computers. These and related sensor technologies are made possible by the ability to engineer magnetic layers on a nanoscale. The need for robust, high-density memories with fast access times continues to drive the search for new magnetic materials and novel growth geometries (1). Promising advancements include the discovery of giant magnetoresistance (GMR) (2) in transition-metal multilayers and "colossal" magnetoresistance (CMR) (3) in perovskite thin films, the design of magnetic spin valves (4) with exchange-biased layers, and the observation and optimization of spin-dependent tunneling (5) across insulating layers.

The first magnetic multilayers were grown by evaporation over 40 years ago (6), but inhomogeneous deposition and extensive interlayer interdiffusion limited their utility for computer storage applications. By the early 1980s, the development of controlled growth techniques, such as sputtering deposition and molecular beam epitaxy (MBE), facilitated the growth of single-crystalline multilayers with well-defined interfaces. Here we describe recent studies of thin films and multilayers composed of rare-earth metals, transition metals, magnetic semiconductors, and/or transition-metal oxides. We restrict our discussion to epitaxial (i.e., single crystalline) systems because the interpretion of the effects of crystallographic orientation, interlayer intermixing, and epitaxial strain is more straightforward.

In order to exploit potential applications of artificially layered materials, a fundamental understanding of magnetic interactions on atomic length scales is essential. The magnetic properties of the component materials in these multilayers are substantially altered from those of bulk due to interlayer exchange coupling, proximity effects, reduced dimensionality, epitaxial strain, and modification of the band structure (7). Both the structural and magnetic characteristics of these magnetic layers can be readily accessed using a wide range of complementary experimental techniques. For example, the structural characteristics are usually determined from x-ray diffraction and microscopy measurements. Resistivity techniques are useful for the identification of anomalous transport behavior, such as GMR and CMR. Magnetometry and magneto-optical Kerr effect (MOKE) measurements provide information about the average magnetic structure and are well suited for samples with ferromagnetic layers. Resonance techniques such as ferromagnetic resonance (FMR) and nuclear magnetic resonance (NMR) probe the local magnetic environment, and microscopy techniques such as scanning electron microscopy with polarization analysis (SEMPA) and magnetic force microscopy (MFM) are sensitive to the surface domain structure. Polarized neutron reflectivity (PNR) yields the magnitude and orientation of the magnetic moment through the buried layers as a function of depth. In general, complex antiferromagnetic spin structures with no net moment can be directly characterized using both high- and low-angle neutron diffraction techniques. Since these details can only be inferred from other experimental techniques, we focus here on the application of neutron diffraction and related scattering techniques to the study of epitaxial magnetic layers.

NEUTRON SCATTERING FROM THIN FILMS

From a historical perspective, neutron scattering has proven itself to be the definitive method for obtaining the detailed microscopic magnetic structure and dynamics of materials in bulk quantities (8,9). It has been demonstrated, more recently, that elastic neutron reflectivity measurements at glancing angles of incidence can also be used to determine both the absolute magnitudes and orientations of ordered configurations of atomic moments in thin films and multilayers. Specifically, polarized neutron reflectivity, measured as a function of the glancing angle of incidence, yields the in-plane component of the vector magnetization depth profile with nanometer spatial resolution. This is due, in part, to the vectorial nature of the interaction between the neutron's magnetic moment and that of the atoms in the material, as will be summarized in this section.

Theoretical Interpretation

One of the greatest advantages of neutron scattering is that the interaction of the neutron with the nucleus and atomic magnetic moment is relatively simple, being described by scattering lengths. The coherent nuclear scattering length b is, in effect, a single average scalar quantity if we assume a random or disordered population of nuclear spin orientations. The coherent magnetic scattering length p is proportional to the magnitude of the atomic magnetic moment (and is dependent on scattering angle). The coherent scattering of neutrons by a collection of ordered magnetic moments also depends upon the relative orientations of the neutron polarization vector, the atomic magnetic moment, and the wave-vector transfer in the scattering process. A detailed description of these fundamental interactions is given in Ref. 8. Because of the vectorial nature of this magnetic interaction, it is possible to obtain, in addition to its magnitude, the orientation of the atomic magnetic moment from polarized neutron scattering (PNS) data.

In Fig. 1 is shown a typical geometry for the specular elastic scattering of polarized neutrons from a series of atomic reflecting planes, some of which are magnetic. Over the lateral coherence length of the incident neutron plane wave, the individual in-plane projections of the atomic moment vectors that contribute to a coherently reflected plane wave are effectively averaged. The neutron polarization is, in this particular case, taken to be along a vertical axis with either spin "+" (up) or "−" (down) perpendicular to the wave-vector transfer $\boldsymbol{Q}$. Any out-of-plane component of the magnetization does not contribute to the scattering. In this particular geometry, the projection of a given plane's magnetization onto the vertical axis gives rise to non-spin-flip (NSF) scattering of the neutron (which can interfere with the nuclear scattering), whereas a projection onto the horizontal axis creates spin-flip (SF) scattering (which does not interfere with the nuclear scattering). From the elastic, specular (angle of incidence equal to angle of reflection) reflection of neutrons information about the chemical composition and vector magnetization depth profiles along the normal to the film surface can be obtained. To obtain information about variations of these quantities in a plane parallel to the surface, off-specular scattering must be measured in which a component of the wave-vector transfer is parallel to that plane. In this case the expressions for the reflectivity necessarily become dependent upon the in-plane components of $\boldsymbol{Q}$ and the spatial coordinates orthogonal to z as well. For the remainder of this subsection, only specular reflectivity will be discussed, for simplicity.

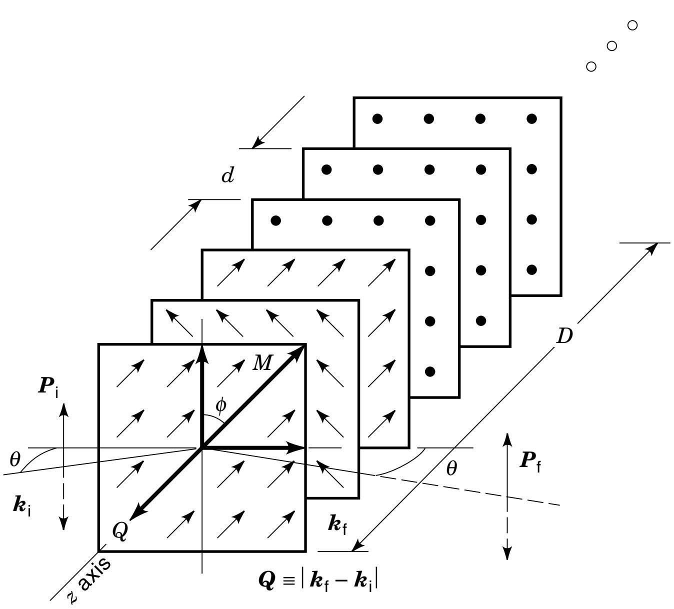

Figure 1. Elastic specular scattering geometry for a single crystalline superlattice. P is the neutron polarization vector, k the neutron wave vector, and Q the wave-vector transfer (the subscripts i and f refer to incident and final states, respectively). The distances d and D correspond to interatomic plane spacing and chemical bilayer thickness, respectively. M is the net in-plane magnetization of an atomic plane and is proportional to the magnetic scattering length p. (After Ref. 12, with permission from Elsevier Science.)

Spin-dependent reflectivities (ratio of reflected to incident intensity) corresponding to NSF (++) and (−−) and SF (+−) and (−+) processes can be measured as a function of angle of incidence or wave-vector transfer $\boldsymbol{Q}$ (e.g., for (− +), the − and + refer to the neutron polarization state before and after scattering from the sample). From such data the vector magnetization depth profile can be reconstructed. It is useful to separate the range of wave-vector transfer into two parts, one at lower $\boldsymbol{Q}$ (and relatively high reflectivity), where the scattering medium can be treated as a continuum, and the other at higher $\boldsymbol{Q}$ (and relatively low reflectivity), where the discrete nature of the atomic planes becomes manifest. It is convenient, then, to refer to PNS as polarized neutron reflectivity (PNR) in the low-$\boldsymbol{Q}$ regime and as polarized neutron diffraction (PND) at high $\boldsymbol{Q}$. For more extensive discussions of the theory of PND and PNR, see, for example, Refs. 8, 10 and Refs. 11, 12, respectively.

Experimental Methods

A schematic representation for carrying out PNR or PND is pictured in Fig. 2. A monochromatic neutron beam can be efficiently polarized by a magnetic supermirror of the type first proposed by Mezei (13) that makes use of the interference between nuclear and magnetic scattering from a magnetic multilayer film to reflect predominantly only one spin state with respect to a fixed magnetic guide field or quantization axis. The use of a series of separate but adjacent magnetic field regions with well-defined, sharp boundaries (across which the neutron polarization vector makes a sudden transition) makes it possible to select the initial and to analyze the final neutron polarization vectors. Within the regions preceding and following the sample, an applied magnetic field can be defined in any direction by appropriate contributions from three mutually orthogonal components as supplied, for example, by three intersecting, perpendicular, rectangular solenoidal wire coils. The neutron polarization can then be made to precess adiabatically to any desired orientation prior to entering the adjacent field region. This method for rotating the neutron polarization was introduced by Rekveldt (14). In the

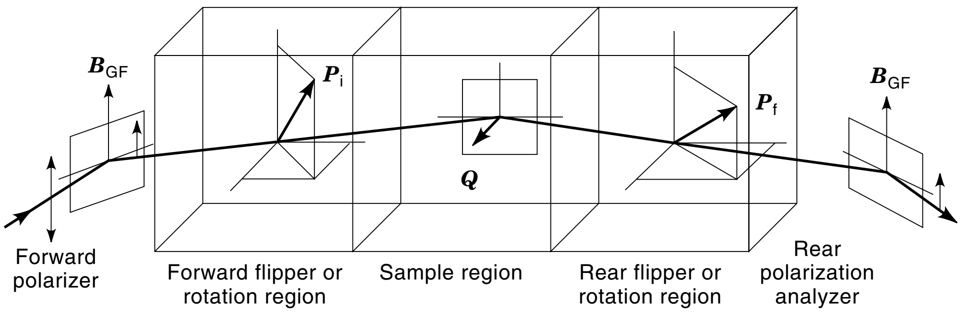

Figure 2. Schematic representation of experimental setup for selecting polarization of incident neutron beam and analyzing polarization of beam scattered by a sample. (After Ref. 12, with permission from Elsevier Science.)

majority of cases, it suffices to align the polarization of the incident neutrons and analyze that of the scattered neutrons as either "up" or "down" along a common direction. Thus, only SF and NSF processes pertaining to the initial and final neutron spin eigenstates are observed.

If the sample is an antiferromagnet, whether collinear or not, the net magnetization is zero and no field need be applied in the sample region (in practice, a relatively small magnetic guide field is often applied to unambiguously define a direction for the polarization axis of the neutrons). Nor does a field need to be applied if the sample is a remanent, single-domain ferromagnet. If, on the other hand, the sample is a multidomain ferromagnet, then a saturating external magnetic field must be applied to avoid depolarization of the neutrons. Both neutron polarizers and flippers have efficiencies that are typically greater than 95%, particularly for PNR experiments in which the angular divergences and spatial dimensions of the beam are relatively small. Nonetheless, for accurate, quantitative measurements, corrections for the imperfect instrumental polarizing and flipping efficiencies are sometimes necessary. (For a discussion of how these corrections are made, see, for example, Ref. 12.) Although the greatest limitation of neutron scattering techniques may be the relatively low intensities currently available, compared to that produced at X-ray synchrotron sources, for instance, numerous polarized neutron reflectometry experiments have been successfully performed on magnetic thin film and multilayer systems that have volumes of only a few millionths of a cubic centimeter, as illustrated by the examples presented in the following.

RESEARCH REVIEW

During the last 15 years, a wide variety of magnetic materials have been grown in thin-film and multilayer geometries. Possible combinations are limited only by the capabilities of modern deposition techniques. Many studies have focused on simple superlattices with alternating magnetic and nonmagnetic layers that were designed to probe the interlayer magnetic coupling for materials with long-range (e.g., rare earths and transition metals) and short-range (e.g., magnetic semiconductors and transition-metal oxides) exchange interactions. These investigations demonstrate the delicate interplay between chemical structure and magnetism.

We review here recent research involving the determination of the magnetic structure in several types of epitaxial magnetic multilayers using polarized and unpolarized neutron diffraction techniques. This survey is not exhaustive, but instead highlights studies that advanced the understanding of fundamental magnetic interactions and inspired the design of more complex and technologically important materials.

Rare-Earth Films and Superlattices

The discovery that yttrium grows epitaxially on the [110] surface of a niobium buffer layer (15) facilitated the deposition of single-crystalline rare-earth films and superlattices by MBE techniques. Exchange coupling of ferromagnetic layers across nonmagnetic interlayers was first reported for *c*-axis Gd/Y superlattices examined by polarized neutron diffraction (16). Specifically, the presence of half-order superlattice reflections in growth-axis scans through the (002) structural reflection (Fig. 3) indicated that the Gd layer moments are sometimes aligned antiparallel across the intervening yttrium. Complementary magnetization measurements (17) showed that the remanent moment and saturation field have an oscillatory dependence on the Y layer thickness. The oscillatory nature of the interlayer exchange interaction was explained as a conse-

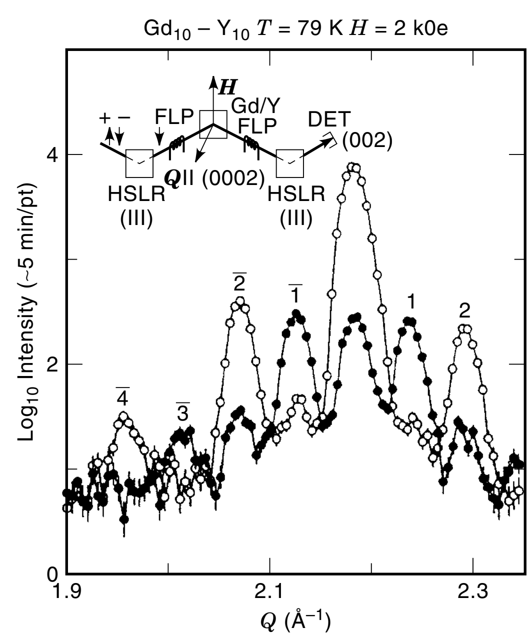

Figure 3. NSF (open circles) and SF (filled circles) scattering from a $[Gd_{10}/Y_{10}]_{225}$ superlattice (the data shown here are not corrected for instrumental polarizing and flipping efficiencies). The SF scattering, which appears at values of Q corresponding to a doubling of the chemical bilayer spacing (odd-numbered satellites), is consistent with an antiparallel alignment of successive ferromagnetic Gd layers. (After Ref. 12, with permission from Elsevier Science.)

quence of Ruderman–Kittel–Kasuya–Yosida (RKKY) coupling of the Gd moments through the conduction band of the nonmagnetic Y layers, which is enabled by nesting features in the Fermi surface (18).

Concurrent with the Gd/Y studies, neutron diffraction investigations of *c*-axis Dy/Y superlattices (19,20) indicated that the phase and chirality of the basal-plane magnetic spiral in bulk dysprosium are also preserved through many superlattice bilayers. The coherence length of the spin ordering was found to decrease with increasing Y layer thickness (20), but the interlayer coupling persists for Y layers thicker than 12 nm. The nonmagnetic rare-earth lutetcium also supports coherent propagation of the Dy spiral ordering (21), but scandium does not (22). This behavior suggests that the nesting features in the Sc Fermi surface are very different from those for Y or Lu.

The effective propagation angle for the spin ordering through the Y layers (20,23–25) is approximately 52°/atomic plane independent of temperature and layer thickness, whereas the Lu propagation angle (23,26) is 40° to 45°/atomic plane. These observations inspired a model (20) for the long-range exchange interactions based upon the stabilization of a spin density wave in the Y or Lu conduction bands via RKKY coupling to the magnetic component. This model was supported by the direct detection of a spin density wave in the Lu constituent of a $Dy_{0.6}Lu_{0.4}$ alloy film using magnetic x-ray scattering techniques (27).

Related studies of *c*-axis Ho/Y (23,24), Ho/Lu (26), and Er/Y (25) showed that the phase information for more complex rare-earth spin structures is also preserved across nonmagnetic interlayers. Similar to Dy, bulk Ho has a basal plane spiral spin structure, but the moments tend to bunch about the six growth-plane easy axes to form "spin-slip" structures (28). While the Ho spiral is coherent across the nonmagnetic blocks in Ho/Y and Ho/Lu superlattices, the "spin-slips" are not correlated in successive Ho layers (24,26). Both the *c*-axis modulated (CAM) and basal-plane spiral spin structures are long range in Er/Y superlattices (25) with Y layer thicknesses less than 10 nm, as demonstrated in Fig. 4.

The nature of the interlayer exchange coupling in rare-earth superlattices, however, is strongly dependent on the growth direction. For *a*- and *b*-axis Dy/Y superlattices grown on Y single crystals, the spiral order is confined to a single Dy interlayer (29). In addition, the strength of the interlayer antiferromagnetic coupling in *b*-axis Gd/Y superlattices (30), determined from the saturation fields, is significantly weaker than that for comparable *c*-axis samples (17). The range of the RKKY exchange interaction is greatly reduced along the *a*- and *b*-axis directions relative to that along the *c* axis.

Because the magnetic phase transitions in the bulk rare earths are driven by changes in the magnetoelastic energy (31), the magnetic properties of these superlattices are very sensitive to strain induced by epitaxial growth. In particular, the Dy basal-plane lattice is smaller than the Y lattice, but larger than the Lu lattice. Epitaxial growth of *c*-axis Dy/Y superlattices thus induces an expansive strain in the Dy basal plane. As a result, the first-order ferromagnetic transition that occurs in bulk Dy (T_C = 178 K) is completely suppressed and the spiral phase angles are larger than that in bulk (20). [Similar behavior is observed in Er/Y superlattices and Er/Y bilayers (25).] In Dy/Lu superlattices, the compression of the Dy lattice in the basal plane leads to an enhancement of the Curie temperature and a reduction of the Dy phase angle (21). The ferromagnetic ordering temperature for 5 nm thick Dy films can be smoothly tuned by growth on Y_xLu_{1-x} base layers with different compositions (32), as shown in Fig. 5. The magnetic properties of Ho-based superlattices also tend to track the induced strain. The Ho propagation angle is larger than that in bulk for Ho/Y superlattices (24) and smaller than that in bulk for Ho/Lu superlattices (26). In the Ho/Lu samples with thin Ho layers, a phase transition occurs to a basal-plane ferromagnetic state that was not previously observed in bulk Ho (26). In general the dependence of the ferromagnetic ordering temperature (20,33,34) and the phase angle (25) on strain can be described by a phenomenological magnetoelastic model.

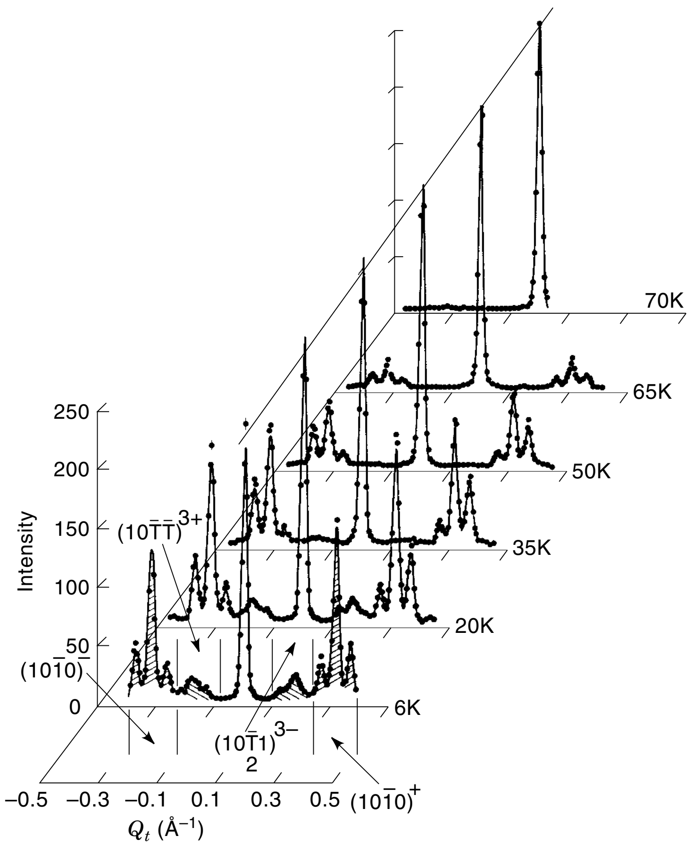

Figure 4. Neutron diffraction scans along the [10$\bar{1}l$] direction for a $[Er_{23.5}/Y_{19}]_{100}$ superlattice. The CAM magnetic satellites and superlattice sidebands are labeled $(10\bar{1}0)^+$ and $(10\bar{1}0)^-$. $(10\bar{1}\bar{1})^{3+}$ and $(10\bar{1}1)^{3-}$ are the third-order magnetic satellites of the (1 0 1 1) and (1 0 1 1) reflections, respectively. The narrow linewidths of all the magnetic satellites reveal that the CAM order is coherent through several superlattice bilayers. (After Ref. 26.)

Other directions in rare-earth research include the growth and characterization of superlattices with two magnetic components, such as Gd/Dy (Ref. 35), Ho/Er, and Dy/Er. The resultant magnetic structures are complex and cannot be explained using simple models describing the bilayer components. For Dy/Er (Ref. 36) and Ho/Er superlattices (Ref. 37), the Ho and Dy magnetic structures propagate through the paramagnetic Er layers at temperatures above T_N = 78 K for the Er layers. The growth-axis coherence length of the spin spiral steadily decreases with temperature as the

Er orders. Below 78 K, the Er CAM in Ho/Er superlattices (37) does not couple across the intervening Ho layers. The difference in the coherence lengths of the CAM and spiral spin structures is evidenced by a two-component line shape in growth-axis scans through the (101) magnetic reflections, as shown in Fig. 6.

More recent studies have focused on superlattices containing light rare-earth metals, such as Nd, which exhibit complex magnetic structures with multiple periodicities. Alloying and strain can dramatically alter the spin structures in bulk due to the delicate balance among indirect exchange interactions and crystal-field effects. In superlattice form, Nd has been combined with nonmagnetic Y (Ref. 38) and Pr (Ref. 39). The complexity of the resultant spin structures cannot readily be explained and requires additional investigation.

Transition-Metal Multilayers

Studies of heavy rare-earth superlattices provided a basis for understanding the anomalous electronic and magnetic behavior of transition-metal multilayers comprised of magnetic and nonmagnetic layers. Initially, light scattering experiments (40) on Fe/Cr multilayers suggested that the ferromagnetic Fe layer moments are aligned antiparallel across the intervening Cr layers in small magnetic fields. This result was directly confirmed by the presence of a half-order magnetic reflection in neutron reflectivity and diffraction data for Fe/Cr (Refs. 41–43), Co/Cu (Ref. 44), and Ni/Ag (Ref. 45) multilayers. These and related (46) antiferromagnetically coupled multilayers exhibited the GMR (giant magnetoresistance) effect (2), characterized by a substantial decrease in the resistivity upon aligning the ferromagnetic layers in a large field (e.g., Fig. 7). Magnetization (47), resistivity (47), and reflectivity (48) measurements revealed that the magnitude of the GMR and of the antiferromagnetic interlayer coupling exhibits an oscillatory dependence on the thickness of the nonmagnetic layers, analogous to the behavior of Gd/Y superlattices (17). The oscillatory exchange interaction was again explained in terms of an RKKY-like coupling mediated by the nonmagnetic layer (49).

Theoretical studies also predicted that the interlayer coupling should be anisotropic and depend on growth direction, as was observed for rare-earth superlattices (29,30). Specifically, the coupling in Cu-based multilayers was expected to be greater along ⟨100⟩ and ⟨110⟩ than along ⟨111⟩ (49). Bulk magnetization measurements of sputtered (111) Co/Cu multilayers (50) showed evidence of strong, oscillatory interlayer coupling, while (111) MBE-grown samples (50–52) did not exhibit antiferromagnetic coupling for Cu thicknesses greater than 1.2 to 1.5 nm. To reconcile these discrepancies, it was suggested that most MBE samples have pinholes through the nonmagnetic Cu layers that shunt any intrinsic antiferromagnetic coupling. The controversy was partially resolved by polarized neutron reflectivity measurements on a series of MBE-grown (111) Co/Cu superlattices (53), as shown in Fig. 8. A distinct, half-order reflection is evident for a

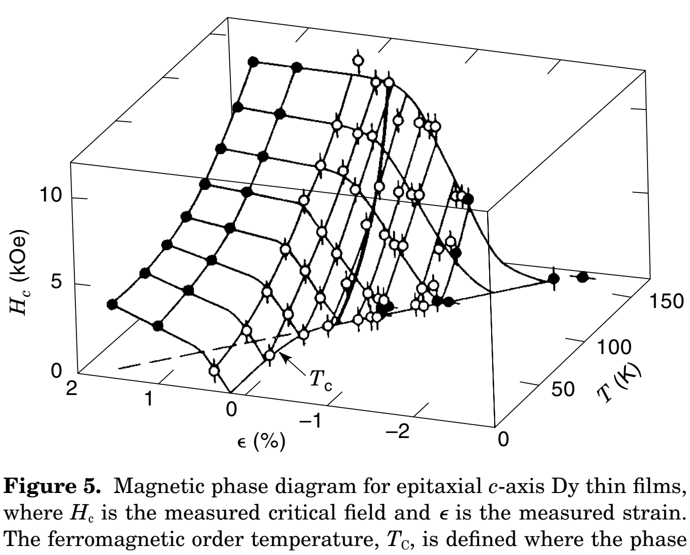

Figure 5. Magnetic phase diagram for epitaxial c-axis Dy thin films, where H_c is the measured critical field and ϵ is the measured strain. The ferromagnetic order temperature, T_C, is defined where the phase boundary intersects the T-ϵ plane at zero field. The open circles are from $(Y_xLu_{1-x})_{1500\,Å}/Dy_{50\,Å}/(Y_xLu_{1-x})_{100\,Å}$ sandwich films and the closed circles are data from related Dy films on Y or Lu base layers. The surface defined by the points marks the transition between the spiral and ferromagnetic spin states. (After Ref. 32.)

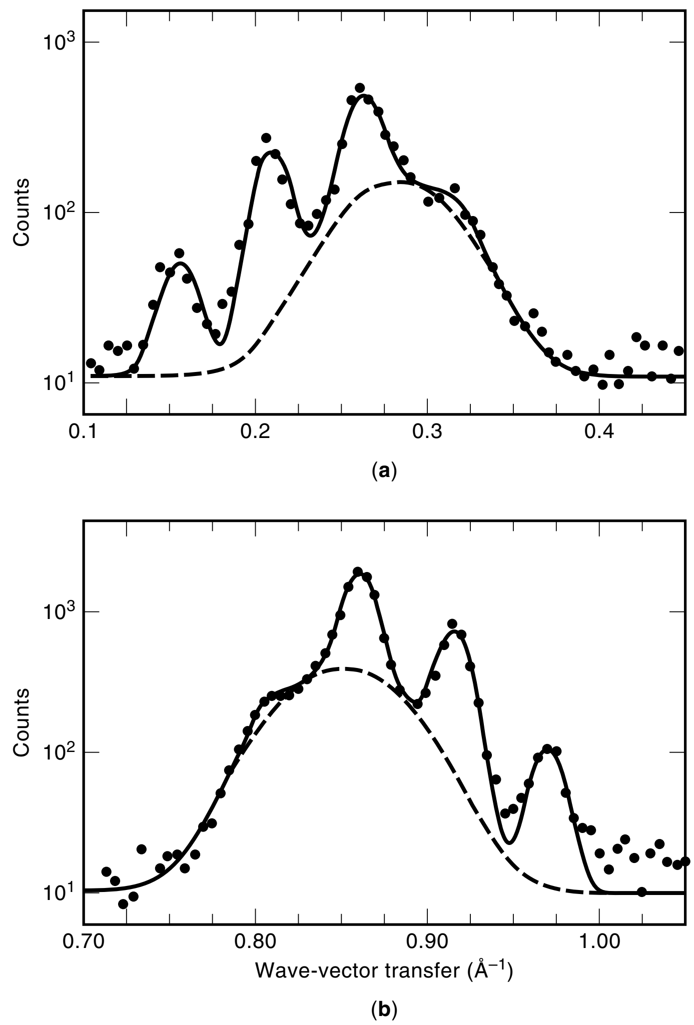

Figure 6. Neutron scattering observed from a Ho_{20}/Er_{22} superlattice at 8 K. The [10l] scans through the Q^- (a) and Q^+ (b) magnetic satellites have been fit with a combination of sharp (solid lines) and broad (dashed lines) Gaussian peaks. The broad peaks have a real-space correlation length equal to the thickness of the Er block (≈6 nm). (After Ref. 37.)

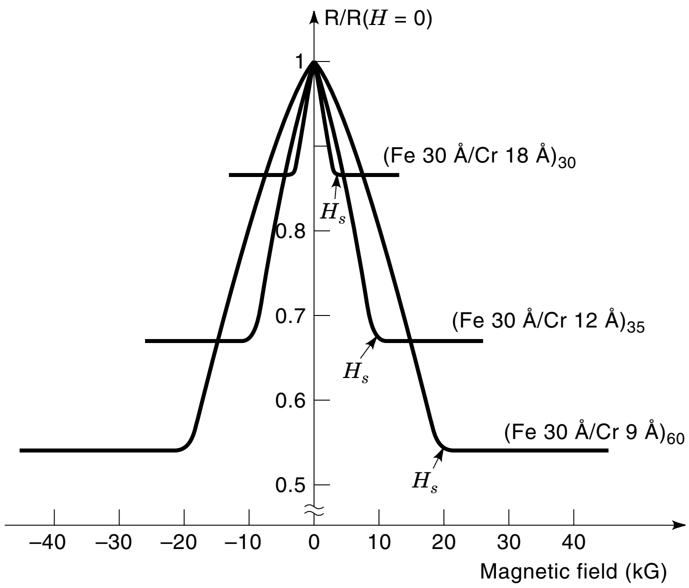

Figure 7. Magnetoresistance of three Fe/Cr superlattices at 4.2 K. The current and the applied field are along the same [110] axis in the plane of the layers. (After Ref. 2.)

The low-field magnetic structure of GMR multilayers, however, can deviate substantially from a simple parallel or antiparallel alignment of the ferromagnetic layers across the nonmagnetic spacer layer. Kerr microscopy (60) and MOKE (61) studies of Fe/Cr multilayers suggested that the Fe moments in neighboring layers are oriented at an angle of 90°. The physical origin of this biquadratic coupling is unknown, though several mechanisms, including spin frustration from interfacial roughness (62) or layer thickness variations (63), have been proposed. The observation of noncollinear spin structures in Fe/Cr (Refs. 64–66) and $Ni_{80}Fe_{20}$/Ag (Ref. 67) multilayers was directly verified by neutron reflectivity techniques. The advantage of neutron reflectivity for these investigations is that the exact angle between the magnetic layers can be determined from fits to the antiferromagnetic and ferromagnetic peak intensities. For example, a neutron study (64) of (001) Fe(5.2 nm)/Cr(1.7 nm) superlattices showed that the low-field angle between the Fe layers is 50°, rather than the expected 90°, for a sample deposited at elevated temperatures [Fig. 10(a)]. For a similar sample grown at room temperature, the Fe moments are fully aligned [Fig. 10(b)] presumably due to differences in the roughness of the superlattice interfaces.

multilayer with 2 nm Cu interlayers. Subsequent fits to the data indicated unambiguously that 15% of the Co spins in this sample are antiferromagnetically coupled across the Cu interlayers. MOKE measurements confirmed that the interlayer coupling has an oscillatory dependence on the Cu thickness, as expected from theory (49).

In general, the magnitude of the GMR and of the saturation fields for transition-metal multilayers are highly sensitive to growth conditions. Post-growth heat treatments can be used to tune and control structural properties such as the grain size and the interfacial intermixing. Low-field GMR was, in fact, induced by low-temperature annealing for a series of $Ni_{83}Fe_{17}$/Cu multilayers prepared by electron-beam evaporation (54). Neutron reflectivity measurements (55) on a series of $[Ni_{83}Fe_{17}(2.7\ nm)/Cu(3.7\ nm)]_{10}$ multilayers confirmed that the permalloy layers are uncoupled or ferromagnetically coupled before annealing and antiferromagnetically coupled after annealing at 300°C or 325°C, as evidenced by a half-order reflection that appears only in low fields (Fig. 9). The antiferromagnetic spin structure is thus directly responsible for the induced GMR. In an attempt to maximize the GMR and minimize the saturation fields of metallic multilayers for possible disk read head applications, a group at IBM grew discontinuous $Ni_{80}Fe_{20}$/Ag multilayers that showed a similar enhancement in the GMR after heat treatments (56). Transmission electron microscopy (TEM) (57) and x-ray diffraction analysis (57,58) revealed that the Ag diffuses into the $Ni_{80}Fe_{20}$ layers at the grain boundaries upon annealing, forming an array of magnetic "islands" in a "sea" of Ag. Specular and off-specular neutron reflectivity measurements (59) indicated that annealing promotes the formation of planar ferromagnetic domains (1 to 10 μm) within each $Ni_{80}Fe_{20}$ layer that are correlated antiferromagnetically along the growth-axis direction. This antiferromagnetic order extends only through a few superlattice bilayers and presumably develops due to weak dipolar coupling among the $Ni_{80}Fe_{20}$ islands.

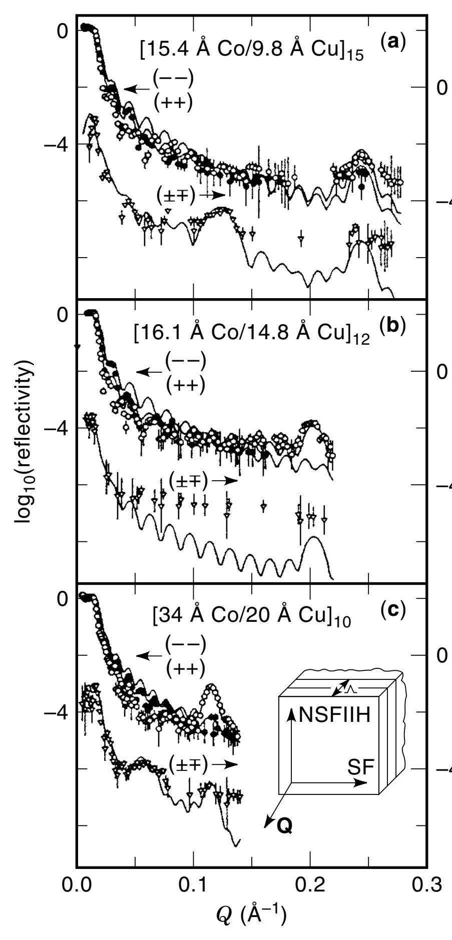

Figure 8. PNR data for three Co/Cu multilayers. All four cross sections are shown. The presence of a half-order reflection in the SF data for (a) and (c) indicate that at least a portion of the Co moments are aligned antiparallel across the intervening Cu layers. (After Ref. 53.)

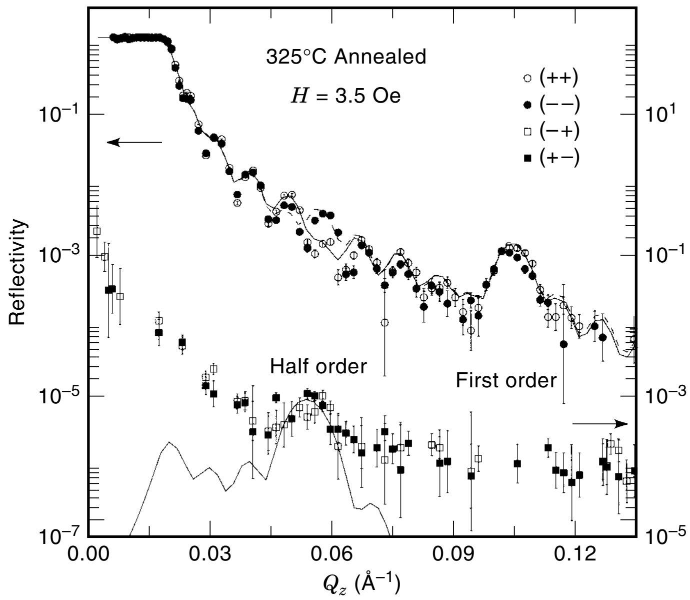

Figure 9. PNR data for a $Ni_{83}Fe_{17}$(2.7 nm)/Cu(3.7 nm) multilayer annealed at 325 °C in a field of 3.5 Oe. The half-order reflection, evident in the NSF and SF cross sections, indicate that the Ni-Fe moments are aligned antiparallel across the nonmagnetic Cu layers. The lines correspond to a fit assuming that the in-plane moments are oriented at an angle of 45° relative to the applied field. (After Ref. 55.) Reprinted with permission. Copyright 1997 American Institute of Physics.

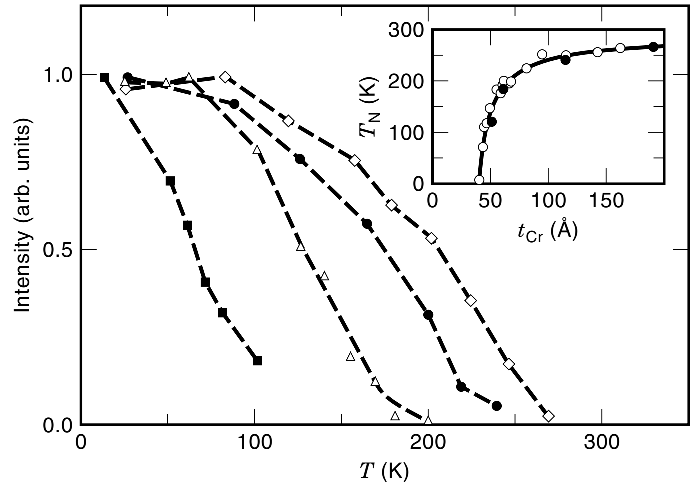

Figure 11. Temperature dependence of the (0 0 1±δ) magnetic reflections for a series of Fe/Cr(t_{Cr} Å) multilayers with t_{Cr} = 190 (open diamonds), 115 (filled circles), 63 (open triangles) and 51 (filled squares). The inset shows the magnetic order temperature, T_N, determined from the neutron data (filled circles) and compared to resistivity results. (After Ref. 68.)

The nature of the interlayer coupling in Fe/Cr multilayers is correlated with the magnetic ordering of the Cr interlayers, which was characterized directly using high-angle neutron diffraction techniques (68,69). The Cr layers in Fe/Cr multilayers support an incommensurate spin density wave (SDW) similar to bulk Cr. The Néel temperature of the Cr SDW was extracted from the temperature dependence of the magnetic (0 0 1 ± δ) Cr reflections (68), as shown in Fig. 11. T_N systematically decreases below T_N = 311 K for bulk Cr as the thickness is reduced to approximately 5 nm. Below this thickness, the incommensurate SDW is completely suppressed (68), and the Cr orders instead as a commensurate antiferromagnet (69). Neutron reflectivity and MOKE measurements revealed that the Fe layers exhibit noncollinear interlayer coupling above T_N in samples with Cr layer thicknesses greater than 5 nm. The formation of the Cr SDW below T_N destroys this interlayer coupling (68,70). Magnetic frustration arising from local interfacial roughness may account for the modification of the magnetic properties of the Cr layers from that of bulk (68) and thus give rise to the anomalous coupling between the Fe layers (62,63).

Additional qualitative details of the Fe magnetic structure in Fe/Cr multilayers were obtained from off-specular neutron reflectivity measurements. Specifically, magnetic diffuse scattering was observed in transverse measurements through the half-order antiferromagnetic reflection for Fe/Cr multilayers that are antiferromagnetically coupled (71,72). The field dependence of this scattering is typified by the data shown in Fig. 12 and is directly correlated with the measured GMR. In general, magnetic diffuse scattering may originate either from the presence of domains across the sample plane or from rough magnetic interfaces (73). It is difficult to distinguish between these two effects, but the increase of the diffuse scattering at the first-order ferromagnetic peak position with applied field in Fig. 12 suggests that this scattering originates from the magnetic disorder at the interfaces (71). For other Fe/Cr (Ref. 72), Co/Ru (Ref. 48), and annealed $Ni_{80}Fe_{20}$/Ag multilayers (Ref. 59), the field dependence of the diffuse scat-

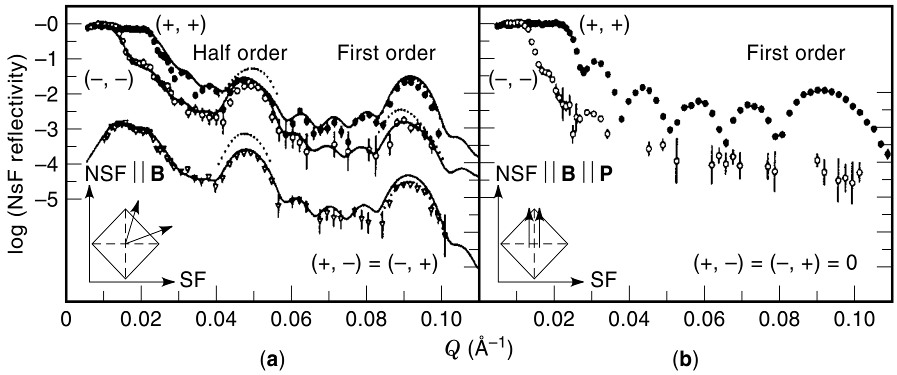

Figure 10. PNR data for Fe(5.2 nm)/Cr(1.7 nm) superlattices grown (a) at elevated temperatures and (b) at room temperature. A 17 Oe field was applied along an easy axis (dashed lines in the insets). In (a), calculations for interlayer coupling angles of 50° (lines) and 90° (small dots) are shown. In (b), the data indicate that the Fe moments are aligned parallel to the field, as shown in the inset. (After Ref. 64.)

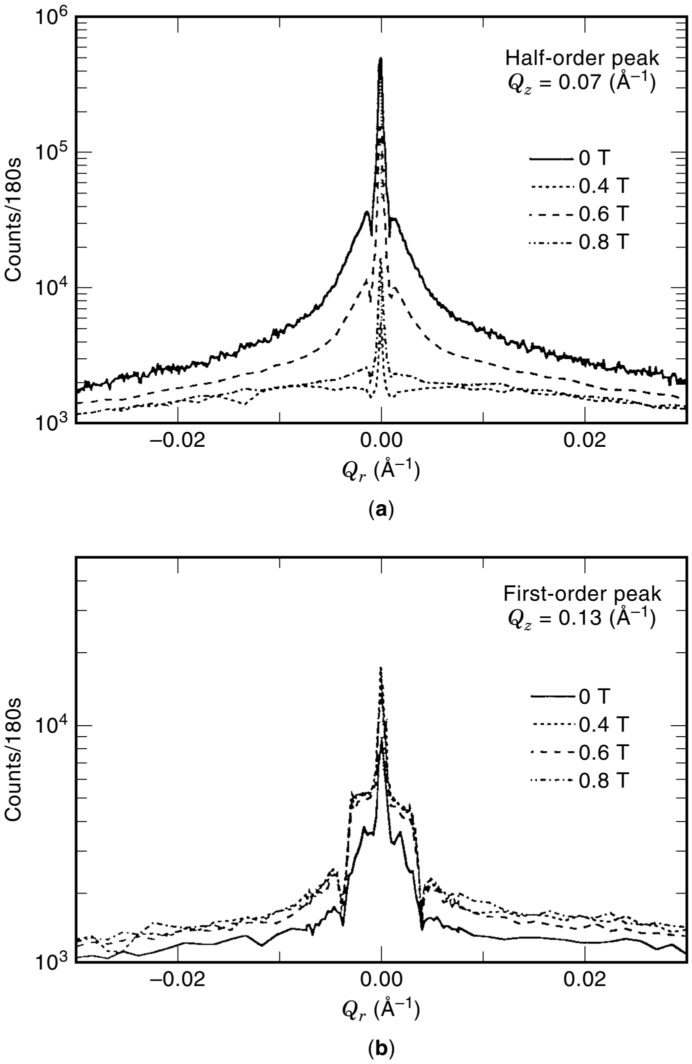

Figure 12. Transverse neutron diffraction scan through the magnetic diffuse scattering at the (a) half-order antiferromagnetic peak position and at the (b) first-order superlattice peak for a Fe(3.0 nm)/Cr(1.0 nm) multilayer. In (a) the diffuse scattering decreases in a large field, whereas in (b) the diffuse scattering increases with field. (After Ref. 71.)

tering is characteristic of in-plane domains within the ferromagnetic layers, ranging in size from 1 to 20 μm. This measurement technique shows great promise for nondestructive analysis of in-plane domains in buried ferromagnetic layers. Research in this area is continuing in an effort to optimize both data collection and analysis capabilities.

Other recent research directions for transition-metal multilayers include studies of hydrogen loading in systems such as Fe/Nb (Ref. 74) and Fe/V (Ref. 75). Due to differences in the hydrogen solubilities of the component materials, the hydrogen goes exclusively into the nonmagnetic interlayers and the exact concentration can be reversibly tuned by changing the pressure. Neutron reflectivity and bulk magnetization measurements of an Fe(2.6 nm)/Nb(1.5 nm) multilayer revealed that increasing the hydrogen concentration to 25 atomic % reverses the interlayer coupling from antiferromagnetic to ferromagnetic (74). Reflectivity studies of Fe/V multilayers (75) also showed a change in the coupling from antiferromagnetic to ferromagnetic and vice versa depending on the V layer thickness, as demonstrated in Fig. 13. These data proved that the transition is not simply caused by the expansion in the V layer thickness induced by hydrogen loading. Instead, it originates from modifications of the Fermi surface in the V interlayers. These studies further emphasize the importance of the Fermi surface in determining the nature of the interlayer exchange coupling in GMR multilayers and suggest another means to isolate desirable magnetic properties.

Magnetic Semiconductor Superlattices

The zinc-blende phase of magnetic semiconductors, such as MnSe and MnTe, has been stabilized by MBE growth of single-crystalline films and superlattices (76–78). Superlattices with alternating magnetic and nonmagnetic interlayers were studied by high-angle neutron diffraction techniques to characterize directly the magnetic behavior associated with this metastable phase and the subsequent effects of confined ge-

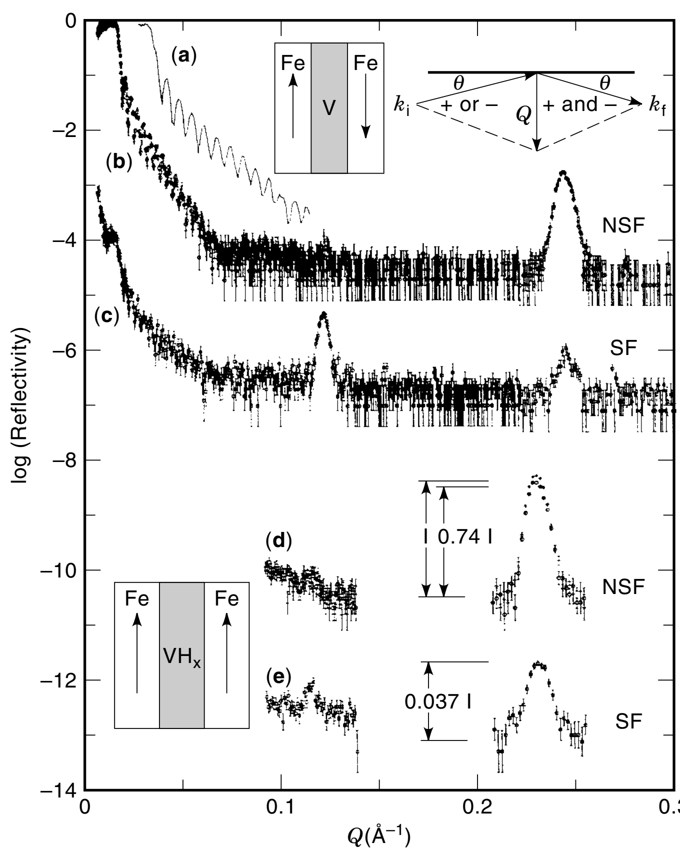

Figure 13. Neutron scattering data for Fe_3/V_{14} as-deposited and hydrogen-loaded samples. These results were obtained at 100 G and room temperature. The inset in the upper right corner shows the PNR geometry. Data (b) represent the NSF components and (c) is the SF components for the as-deposited sample. The curve (a) is the (++) intensity included in (b) expanded by a factor of 2 along the Q axis to show the finite-size oscillations. The data in (d) and (e) are the NSF and SF intensities for a sample exposed to 14 kPa hydrogen pressure. The other insets depict the antiferromagnetic alignment for the as-deposited sample and the ferromagnetic alignment of the hydrogen-loaded sample. (After Ref. 75.)

ometries. Similar to β-MnS and doped alloys of MnSe and MnTe, the magnetic constituents order as type III antiferromagnets (79). The coherence of the antiferromagnetic structure in MnSe/ZnSe (76), MnTe/ZnTe (77), and MnSe/ZnTe (78) superlattices is limited to a single bilayer for thick nonmagnetic layers ($\gtrsim$ 2 nm) since the superexchange interactions in bulk magnetic semiconductors are short range.

By cubic symmetry, the spins in bulk magnetic semiconductors can order in three different types of antiferrimagnetic domains. Neutron diffraction studies of the half-order antiferromagnetic reflections indicated that the spins in MnSe/ZnSe (76) and MnTe/ZnTe (77) superlattices align exclusively in domains with antiferromagnetic sheets parallel to the growth plane. In contrast, the spins in MnSe/ZnTe superlattices (78) align in the other two types of domains that have antiferromagnetic sheets perpendicular to the growth plane. The selection of unique domain orientations in these samples is a direct consequence of epitaxial strain. Specifically, lattice matching compresses the magnetic layers in MnSe/ZnSe and MnTe/ZnTe superlattices in the growth plane and expands the magnetic layers in MnSe/ZnTe superlattices. Tensile strain in MnSe/ZnTe superlattices also stabilized a new helimagnetic phase, as evidenced by the temperature-dependent shift in the position of the antiferromagnetic reflection shown in Fig. 14. The phase advance of the helix showed a pronounced sensitivity to epitaxial strain, which can be qualitatively reproduced using a simple mean-field model that includes only the competing nearest-neighbor and next-nearest-neighbor exchange interactions (78).

More recent neutron diffraction studies of MnTe/CdTe superlattices (80) showed a coexistence of the commensurate antiferromagnetic and incommensurate helical ordering. This behavior may again be a consequence of epitaxial strain, which is much smaller in this superlattice system. In addition, the magnetic order propagates coherently across nonmagnetic interlayers thinner than 3 nm. Long-range magnetic order was also observed in related EuTe/PbTe superlattices (79,81). The mechanism responsible for this interlayer coupling is not known and remains a direction for future investigations.

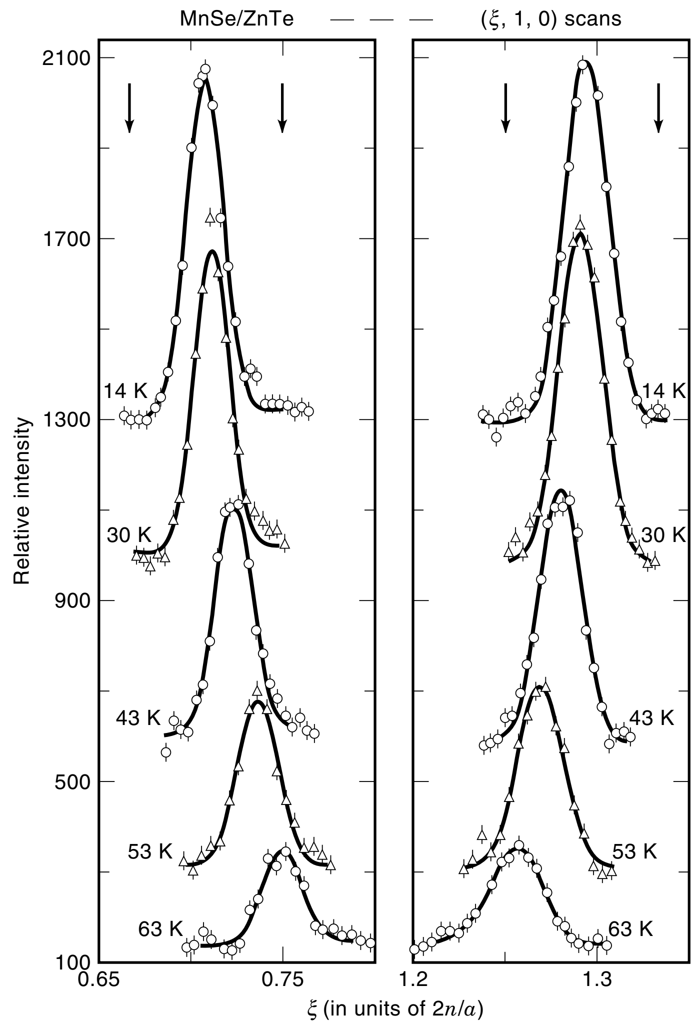

Figure 14. Neutron diffraction scans for a ZnTe/MnSe superlattice along (ψ 1 0) through the magnetic reflections at ($1\pm\delta$ 1 0). The reflections correspond to incommensurate helical order. The vertical arrows show the peak positions corresponding to commensurate helices. (After Ref. 78.)

Transition-Metal Oxide Superlattices

Similar to magnetic semiconductor superlattices, the interlayer exchange interaction between the magnetic components in transition-metal oxide multilayers is short range, as it is governed by superexchange. Early studies of transition-metal oxides focused on multilayers composed of a ferrimagnet and an antiferromagnet (82), such as Fe_3O_4/CoO and Fe_3O_4/NiO, or of alternating antiferromagnets (83,84), such as CoO/NiO. While the multilayers retain a spin structure characteristic of their bulk constituents, the magnetic behavior is strongly perturbed by local coupling at the interfaces.

For example, high-angle neutron diffraction scans for (111) CoO/NiO multilayers (83) showed a narrow ($\frac{1}{2}\frac{1}{2}\frac{1}{2}$) peak, indicating that the collinear antiferromagnetic order is long range and propagates coherently through several bilayers. For samples with thin bilayers (<5 nm), the CoO and NiO antiferromagnetic structures develop simultaneously at a temperature that scales with the relative bilayer composition between their bulk T_N of 290 K and 520 K, respectively. Average order-parameter data for multilayers with thicker bilayers have two distinct anomalies closer to the bulk ordering temperatures (84,85), as demonstrated in Fig. 15. Structure factor fits to data for a $[NiO(4.3\ nm)/CoO(2.9\ nm)]_{100}$ multilayer suggested that the Ni and Co moments in the center of the layers order at distinct Néel temperatures shifted from their bulk values (85). Above 400 K, however, the Ni antiferromagnetic order persists through two bilayers even though the CoO is effectively disordered and the interlayer exchange coupling is short range. More than 3.5 nm of CoO is required to disrupt this interlayer coupling. Mean-field calculations (85,86), which include only nearest-neighbor interactions, qualitatively describe the dependence of the CoO and NiO ordering temperatures on the relative thickness of the components (Fig. 15), but cannot account for the observed coupling across paramagnetic CoO layers.

In related (001) Fe_3O_4/NiO superlattices (87), magnetic proximity effects give rise to similar shifts in the ordering temperatures of the magnetic components. Though these materials grow as single crystals, symmetry differences between the Fe_3O_4 spinel and NiO rocksalt structures give rise to stacking faults at the superlattice interfaces. Even though the structural coherence of the Fe_3O_4 is limited to a single layer, the NiO antiferromagnetic order propagates coherently through several bilayers. The broad scattering from the ferrimagnetic Fe_3O_4 layers can thus be easily separated from the NiO scattering. As demonstrated by the (00l) scan through the (111) reflection in Fig. 16, T_N of the NiO interlayers can be measured directly by tracking the temperature dependence of the narrow component of this magnetic reflection.

Fe_3O_4/NiO (Ref. 88) and Fe_3O_4/CoO (Refs. 82, 89, 90) superlattices, as well as NiO/CoO bilayers capped with $Fe_{81}Ni_{19}$ (Ref. 91), are also technologically important because they exhibit the so-called *exchange-biasing* effect. These and similar layered structures can be used to stabilize magnetic domains in GMR spin-valve read heads and sensors. When exchange-biased multilayers are field cooled through T_N of the antiferromagnet component, the magnetic hysteresis loop is shifted along the field axis as a result of interlayer exchange coupling

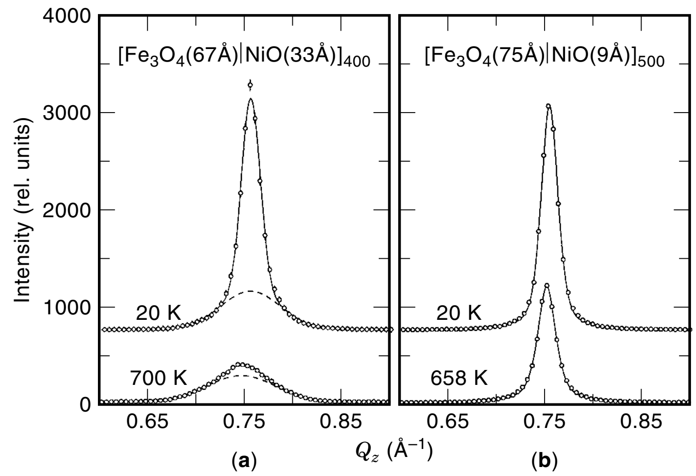

Figure 16. Neutron diffraction scans along the [00l] direction through the (111) reflection for a [Fe_3O_4(67 Å)/NiO(33 Å)]$_{400}$ superlattice at 20 K and 700 K and for a [Fe_3O_4(75 Å)/NiO(9 Å)]$_{500}$ superlattice at 20 K and 658 K. For the former, the broad Gaussian component (dashed line) corresponds to scattering from the Fe_3O_4 interlayers and the narrow Gaussian component arises from the NiO interlayers. The Fe_3O_4 scattering is broadened by structural stacking faults at the superlattice interfaces. (After Ref. 87.)

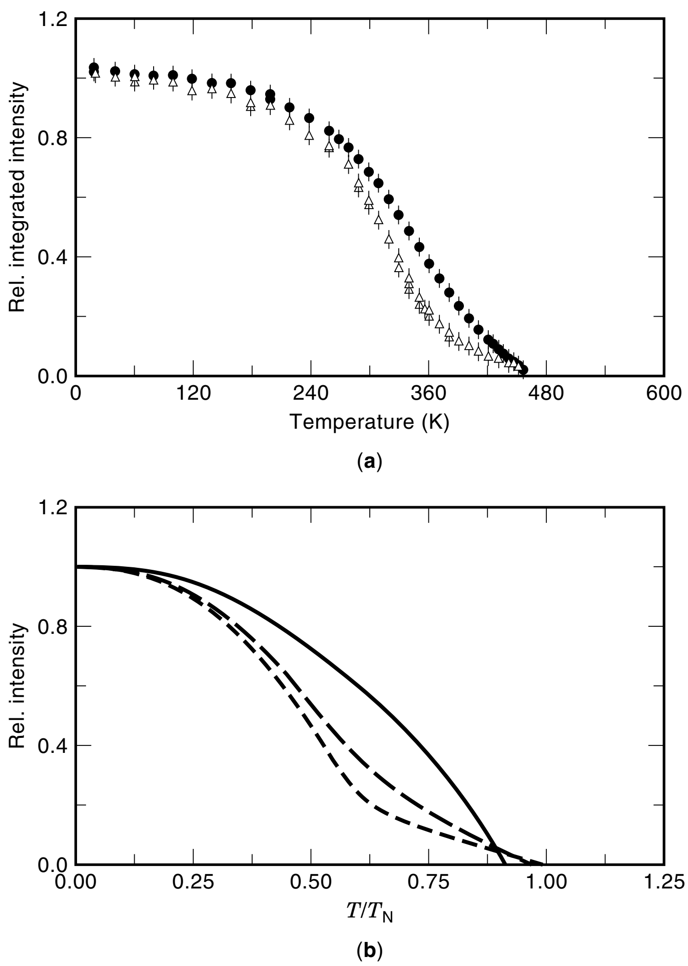

Figure 15. (a) Temperature dependence of the integrated intensity of the $(\frac{1}{2}\frac{1}{2}\frac{1}{2})$ half-order magnetic peak for [NiO(21 Å)/CoO(15 Å)]$_{145}$ (dark circles) and [NiO(43 Å)/CoO(29 Å)]$_{100}$ (open triangles) superlattices. For the thicker sample, the data show changes in curvature near the magnetic ordering temperatures of bulk NiO and CoO. (b) Mean field calculation of the $(\frac{1}{2}\frac{1}{2}\frac{1}{2})$ peak intensity for NiO/CoO bilayers consisting of three (solid line), eight (long dashes), and fifteen (short dashes) atomic planes of both Ni and Co. The calculated temperature dependence is similar to the data in (a). (After Ref. 85.)

between the ferromagnetic (or ferrimagnetic) and antiferromagnetic layers. Though this effect was discovered more than 40 years ago (92), the microscopic origin and specific role of the antiferromagnet are still not completely understood. Early models assumed that the topmost atomic plane of the antiferromagnet has a small net moment (i.e., an “uncompensated” plane) that aligns antiparallel to the ferromagnet upon field cooling (92–94). These models also predicted that domain walls form in the antiferromagnetic layer upon reversing the magnetization from the field-cooling direction (93,94). In fact, neutron reflectivity data suggested that the saturated Fe_3O_4 moment is reduced from bulk near the interfaces in Fe_3O_4/NiO superlattices (88). After field cooling, the reflectivity scans in positive and negative saturating fields differed substantially. These data are consistent with a model in which domain walls form in the ferrimagnetic layers, rather than the antiferromagnetic. High-angle neutron diffraction studies of (001) Fe_3O_4/CoO superlattices (95) focused instead on the field dependence of the antiferromagnetic spin structure. These data showed a 90° orientation between the antiferromagnetic and ferrimagnetic moments that is frozen in upon field cooling. These results thus confirmed the primary prediction of a recent exchange-biasing model (96). Because neutron diffraction provides direct information about the domain structures within antiferromagnetic layers, it is an important tool for the understanding of these exchange-biased multilayers.

CONCLUSION

Research continues in each of the areas described above. While the needs of the magnetic recording and sensor industry have motivated many of the studies to date, more fundamental questions remain regarding the specific role of interlayer coupling, confined geometries, and epitaxial strain.

Future directions include the study of perovskite films and multilayers (3), as well as magnetic tunnel junctions with insulating interlayers (5). Neutron reflectivity and diffraction techniques have been essential tools for preliminary characterization of these devices and promise to provide key information about the spin structures associated with the desirable magnetic characteristics of these materials.

BIBLIOGRAPHY

1. J. L. Simonds, *Phys. Today,* **48**(4): 26–32, 1995.
2. M. N. Baibich et al., *Phys. Rev. Lett.,* **61**: 2472–2475, 1988.
3. S. Jin et al., *Science,* **264**: 413–415, 1994; R. von Helmolt et al., *Phys. Rev. Lett.,* **71**: 2331–2334, 1993.
4. B. Dieny et al., *Phys. Rev. B,* **43**: 1297–1300, 1991.
5. J. Moodera, R. Meservey, and X. Hao, *Phys. Rev. Lett.,* **70**: 853–856, 1993; J. S. Moodera et al., *Appl. Phys. Lett.,* **69**: 708–710, 1996.
6. M. S. Blois, *J. Appl. Phys.,* **26**: 975–980, 1955.
7. L. M. Falicov et al., *J. Mater. Res.,* **5**: 1299–1340, 1990.
8. G. E. Bacon, *Neutron Diffraction,* 3rd ed., London: Oxford University Press, 1975.
9. C. Shull and B. Brockhouse, Nobel Prize 1993.
10. R. M. Moon, T. Riste, and W. C. Koehler, *Phys. Rev.,* **181**: 920–931, 1969.
11. G. P. Felcher et al., *Rev. Sci. Instrum.,* **58**: 609–619, 1987.
12. C. F. Majkrzak, *Physica B,* **221**: 342–356, 1996.
13. F. Mezei, *Commun. Phys.,* **1**: 81–85, 1976.
14. M. Th. Rekveldt, *J. Phys. (Paris) Colloq.,* **1**: 579, 1971.
15. J. Kwo et al., in J. H. Gibson and L. R. Dawson (eds.), *Layered Structures, Epitaxy and Interfaces,* Materials Research Society Symposia Proceedings, Pittsburgh: Materials Research Society, 1985, Vol. 37, p. 509.
16. C. F. Majkrzak et al., *Phys. Rev. Lett.,* **56**: 2700–2703, 1986.
17. J. Kwo et al., *Phys. Rev. B,* **35**: 7295–7298, 1987.
18. Y. Yafet et al., *J. Appl. Phys.,* **63**: 3453–3457, 1988.
19. M. B. Salamon et al., *Phys. Rev. Lett.,* **56**: 259–262, 1986.
20. R. W. Erwin et al., *Phys. Rev. B,* **35**: 6808–6825, 1987; J. J. Rhyne et al., *Physica B* , **159**: 111–128, 1989.
21. R. S. Beach et al., *Phys. Rev. Lett.,* **70**: 3502–3505, 1993.
22. F. Tsui et al., *J. Appl. Phys.,* **73**: 6904–6906, 1993.
23. J. Bohr et al., *Physica B,* **159**: 93–105, 1989.
24. D. A. Jehan et al., *Phys. Rev. B,* **48**: 5594–5606, 1993.
25. J. A. Borchers, *Phys. Rev. B,* **43**: 3123–3126, 1991; J. A. Borchers et al., *ibid.,* **44**: 11814–11824, 1991.
26. P. P. Swaddling et al., *Phys. Rev. B,* **53**: 6488–6498, 1996.
27. B. A. Everitt et al., *Phys. Rev. Lett.,* **75**: 3182–3185, 1995.
28. D. Gibbs et al., *Phys. Rev. Lett.,* **55**: 234–237, 1985.
29. F. Tsui et al., *Phys. Rev. B,* **43**: 13320–13330, 1991.
30. F. Tsui et al., *J. Magn. Magn. Mater.,* **104–107**: 1901–1902, 1992.
31. W. E. Evenson and S. H. Liu, *Phys. Rev.,* **138**: A507, 1965.
32. F. Tsui and C. P. Flynn, *Phys. Rev. Lett.,* **71**: 1462–1465 (1993).
33. J. J. Rhyne and R. W. Erwin, in K. H. J. Buschow (ed.), *Magnetic Materials,* Amsterdam: North-Holland, 1995, Vol. 8, p. 1.
34. K. Dumesnil et al., *Phys. Rev. B,* **53**: 11218–11221, 1996.
35. C. F. Majkrzak et al., *J. Appl. Phys.,* **63**: 3447–3452, 1988.
36. K. Dumesnil et al., *Phys. Rev. B,* **54**: 6407–6420, 1996.
37. J. A. Simpson et al., *Phys. Rev. Lett.,* **73**: 1162–1165, 1994.
38. B. A. Everitt et al., *Phys. Rev. B,* **56**: 5452–5460, 1997.
39. J. P. Goff et al., *J. Magn. Magn. Mater.,* **156**: 263–264, 1996; D. F. McMorrow, *Neutron News,* **7**: 16–20, 1996.
40. P. Grünberg et al., *Phys. Rev. Lett.,* **57**: 2442–2445, 1986.
41. A. Barthélémy et al., *J. Appl. Phys.,* **67**: 5908–5913, 1990.
42. N. Hosoito et al., *J. Phys. Soc. Jpn.,* **59**: 1925–1927, 1990; T. Shinjo, S. Araki, and N. Hosoito, *J. Magn. Magn. Mater.,* **90–91**: 753–757, 1990.
43. S. S. P. Parkin, A. Mansour, and G. P. Felcher, *Appl. Phys. Lett.,* **58**: 1473–1475, 1991.
44. A. Cebollada et al., *Phys. Rev. B,* **39**: 9726–9729, 1989.
45. B. Rodmacq, Ph. Mangin, and Chr. Vettier, *Europhys. Lett.,* **15**: 503–507, 1991.
46. S. S. P. Parkin, *Phys. Rev. Lett.,* **67**: 3598–3601, 1991.
47. S. S. P. Parkin, N. More, and K. P. Roche, *Phys. Rev. Lett.,* **64**: 2304–2307, 1990; S. S. P. Parkin, R. Bhadra, and K. P. Roach, *ibid.,* **66**: 2152–2155, 1991.
48. Y. Y. Huang, G. P. Felcher, and S. S. P. Parkin, *J. Magn. Magn. Mater.,* **99**: L31–L38, 1991.
49. P. Bruno and C. Chappert, *Phys. Rev. Lett.,* **67**: 1602–1605, 1991; *Phys. Rev. B,* **46**: 261–270, 1992.
50. S. S. P. Parkin et al., *Phys. Rev. B,* **46**: 9262–9265, 1992.
51. W. F. Egelhoff, Jr. and M. T. Kief, *Phys. Rev. B,* **45**: 7795–7804, 1992.
52. M. T. Johnson et al., *Phys. Rev. Lett.,* **69**: 969–972, 1992.
53. A. Schreyer et al., *Phys. Rev. B,* **47**: 15334–15337, 1993.
54. A. M. Zeltser and N. Smith, *J. Appl. Phys.,* **79**: 9224–9230, 1996.
55. J. A. Borchers et al., *J. Appl. Phys.,* **81**: 3771–3773, 1997.
56. T. L. Hylton, et al., *Science,* **261**: 1021–1024, 1993; *J. Appl. Phys.,* **75**: 7058–7060, 1994.
57. M. A. Parker et al., *J. Appl. Phys.,* **75**: 6382–6384, 1994; E. Snoeck et al., *J. Magn. Magn. Mater.,* **151**: 24–32, 1995.
58. M. Chládek et al., *J. Appl. Phys.,* **80**: 1437–1445, 1996.
59. J. A. Borchers et al., *Phys. Rev. B,* **54**: 9870–9882, 1996; J. A. Borchers et al., *J. Appl. Phys.,* **79**: 4762–4764, 1996.
60. M. Rührig et al., *Phys. Status Solidi A,* **125**: 635–656, 1991.
61. B. Heinrich et al., *Phys. Rev. B,* **44**: 9348–9361, 1991.
62. S. Demokritov et al., *Phys. Rev. B,* **49**: 720–723, 1994.
63. J. C. Slonczewski, *J. Appl. Phys.,* **73**: 5957–5962, 1993; *Phys. Rev. Lett.,* **67**: 3172–3175, 1991.
64. A. Schreyer et al., *Europhys. Lett.,* **32**: 595–600, 1995; A. Schreyer et al., *Phys. Rev. B,* **52**: 16066–16085, 1995.
65. A. C. Bland et al., *J. Appl. Phys.,* **79**: 6295–6297, 1996.
66. S. Adenwalla et al., *Phys. Rev. B,* **53**: 2474–2480, 1996.
67. B. Rodmacq et al., *Phys. Rev. B,* **48**: 3556–3559, 1993; K. Dumesnil et al., *Physica B,* **213–214**: 245–247, 1995.
68. E. E. Fullerton, S. D. Bader, and J. L. Robertson, *Phys. Rev. Lett.,* **77**: 1382–1385, 1996; E. E. Fullerton et al., *Physica B,* **221**: 370–376, 1996.
69. A. Schreyer et al., *Phys. Rev. Lett.,* **79**: 4914–4917, 1997.
70. J. F. Ankner et al., *J. Appl. Phys.,* **79**: 4782, 1996.
71. M. Takeda et al., *J. Phys. Soc. Jpn.,* **62**: 3015–3018, 1993; M. Takeda et al., *J. Magn. Magn. Mater.,* **126**: 355–357, 1993; M. Takeda et al., *Physica B,* **213–214**: 248–250, 1995.
72. W. Hahn et al., *J. Appl. Phys.,* **75**: 3564–3570, 1994.
73. S. K. Sinha, in D. A. Neumann, T. P. Russell and B. J. Wuensch (eds.), *Neutron Scattering in Materials Science II,* Materials Research Society Symposia Proceedings, Pittsburgh: Materials Research Society, 1995, **376**: p. 175.
74. F. Klose et al., *Phys. Rev. Lett.,* **78**: 1150–1153, 1997; Ch. Rehm et al, *Physica B,* **221**: 377–381, 1996.
75. B. Hjörvarsson et al., *Phys. Rev. Lett.,* **79**: 901–904, 1997.

76. N. Samarth et al., *Phys. Rev. B,* **44**: 4701–4704, 1991.
77. T. M. Giebultowicz et al., *Phys. Rev. B,* **48**: 12817–12833, 1993.
78. T. M. Giebultowicz et al., *Phys. Rev. B,* **46**: 12076–12079, 1992.
79. T. M. Giebultowicz et al., *Physica B,* **198**: 163–168, 1994.
80. V. Nunez et al., *J. Magn. Magn. Mater.,* **140–144**: 633–634, 1995.
81. T. M. Giebultowicz et al., *J. Magn. Magn. Mater.,* **140–144:** 635–636, 1995.
82. Y. Bando and T. Terashima, *Adv. Cer.,* **15**: 607–612, 1985.
83. M. Takano et al., *Appl. Phys. Lett.,* **51**: 205–206, 1987.
84. Y. Bando et al., in M. Doyama et al., (eds.), *Multilayers,* Proc. MRS Int. Meet. Adv. Mater., Pittsburgh: Materials Research Society, 1989, **10**, pp. 83–94.
85. J. A. Borchers et al., *Phys. Rev. Lett.,* **70**: 1878–1881, 1993; J. A. Borchers et al., *J. Appl. Phys.,* **73**: 6898–6900, 1993.
86. A. S. Carrico and R. E. Camley, *Phys. Rev. B,* **45**: 13117–13120, 1992; R. W. Wang and D. L. Mills, *ibid.,* **46**, 11681–11687, 1992.
87. J. A. Borchers et al., *Phys. Rev. B,* **51**: 8276–8286, 1995; J. A. Borchers et al., *Appl. Phys. Lett.,* **64**: 381–383, 1994.
88. A. R. Ball et al., *Appl. Phys. Lett.,* **69**: 1489–1491, 1996; A. R. Ball et al., *Physica B,* **221**: 388–392, 1996.
89. T. Terashima and Y. Bando, *Thin Solid Films,* **152**: 455–463, 1987.
90. P. J. van der Zaag et al., *J. Appl. Phys.,* **79**: 5103–5105, 1996.
91. M. J. Carey et al., *Phys. Rev. B,* **47**: 9952–9954, 1993; M. J. Carey and A. E. Berkowitz, *Appl. Phys. Lett.,* **60**: 3060–3062, 1992.
92. W. H. Meiklejohn and C. P. Bean, *Phys. Rev.,* **105**: 904–913, 1957.
93. D. Mauri et al., *J. Appl. Phys.,* **62**: 3047–3049, 1987.
94. A. P. Malozemoff, *Phys. Rev. B,* **37**: 7673–7679, 1988.
95. Y. Ijiri et al., *Phys. Rev. Lett.,* **80**: 608–611, 1998.
96. N. C. Koon, *Phys. Rev. Lett.,* **78**: 4865–4868, 1997.

J. A. Borchers
C. F. Majkrzak
National Institute of Standards and Technology

MAGNETIC FIELD, EFFECT ON HEAT CONDUCTION.

See Thermal magnetoresistance.